Received 26 April 2026; accepted 17 May 2026. Date of publication 19 May 2026; date of current version 23 October 2026.

Digital Object Identifier 10.1109/OJAP.2026.3694994

Aperture Field Analysis and Mobility-Aware Multiuser Modeling of Multibeam Multipolarized Holographic Metasurface Antennas for Low-Profile SATCOM Transmitters

SWARNADIPTO GHOSH [1,2,3] (Graduate Student Member, IEEE), SUBHADRITA GHOSH [3] (Graduate Student Member, IEEE), AND CHINMOY SAHA [3] (Senior Member, IEEE)

[1]Department of Information Technology, Ghent University, Ghent 9052, Belgium
[2]IMEC, Leuven 3000, Belgium
[3]Department of Avionics, Indian Institute of Space Science and Technology, Thiruvananthapuram 695547, India

CORRESPONDING AUTHOR: SWARNADIPTO GHOSH (e-mail: swarnadipto.2000@gmail.com)

This work was supported by the Indian Institute of Space Science and Technology (IIST), Thiruvananthapuram, India.

ABSTRACT This article presents an in-depth aperture-field analysis and numerical design methodology for multi-beam, multi-polarized holographic metasurfaces (HMS), followed by a system-level evaluation through mobility-aware multiuser modeling. A theoretical EM framework is first developed for aperture-field analysis, and two HMS topologies are designed to generate multiple linearly and circularly polarized beams with prescribed impedance modulation schemes. Building upon this design, a signal-processing-based multiuser analysis is performed, where the metasurface is modeled as a polarimetric channel using an H-matrix framework, enabling spatial- and polarization-division multiple access (SP-PDMA). The system-level study incorporates user mobility and angular misalignment to quantify the impact of beam deviation on SNR and sum-rate performance. The proposed HMS designs, comprising $88 \times 88 = 7744$ scalar meta-unit cells with an overall aperture of $26.5\lambda_0 \times 26.5\lambda_0$, produce quad-beam, multi-planar, multi-polarized radiation at 25 GHz. Design-1 exhibits dual azimuth-plane radiation with dual circularly polarized beams (LHCP and RHCP) at $(\theta_1, \varphi_1) = (-20°, 0°)$ and $(\theta_2, \varphi_2) = (20°, 0°)$, along with dual linearly polarized beams (HP and VP) at $(\theta_3, \varphi_3) = (-20°, 90°)$ and $(\theta_4, \varphi_4) = (20°, 90°)$, making it well suited for SP-PDMA. Design-2 generates four linearly polarized beams (HP or VP) at $(\theta_n, \varphi_n) = \{(20°, 45°), (20°, 135°), (20°, 225°), (20°, 315°)\}$ with a peak gain ($g_{\max}$) better than 26.5 dBi, providing enhanced SNR, reduced inter-user interference, and improved spectral efficiency. Numerical simulations demonstrate that the multi-polarization metasurface outperforms single-polarization configurations in SNR and interference mitigation. Beam misalignment and SNR-loss histograms further quantify mobility-induced performance variations, highlighting the framework's capability to link EM metasurface design with multiuser system performance in high-mobility wireless communication scenarios.

INDEX TERMS Holographic metasurface, modulated metasurface, multibeam, multiuser modeling, polarization division multiple access.

I. INTRODUCTION

MODERN antenna and electromagnetic aperture technologies are becoming an integral requirement to achieve high directivity, multi-beam capability, polarization diversity, and dynamic reconfigurability within stringent size, weight, power, and cost (SWaP-C) constraints. Such requirements arise across a wide range of applications, including satellite communications (SATCOM), sensing and imaging systems, wireless backhaul, and emerging multi-user platforms. Conventional phased arrays, although widely adopted for majority of applications, rely on dense feed networks, phase shifters, and complex calibration procedures, which significantly increase hardware complexity, power consumption, and cost, particularly for large-aperture and

© 2026 The Authors. This work is licensed under a Creative Commons Attribution 4.0 License.
For more information, see https://creativecommons.org/licenses/by/4.0/

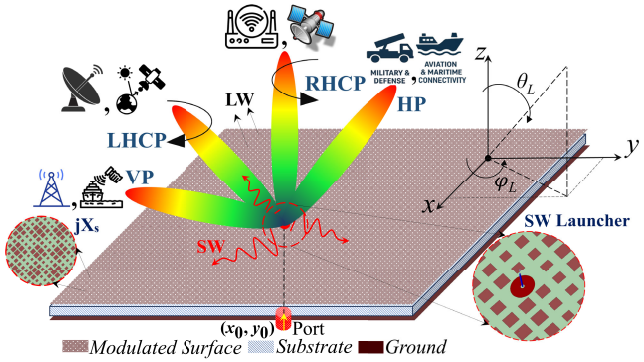


FIGURE 1. Conceptual illustration of multi-polarized multibeam HMS.

multifunctional implementations [1], [2], [3]. These limitations have motivated extensive research into alternative aperture concepts capable of achieving comparable or enhanced electromagnetic functionality with reduced system overhead.

Metasurface-based apertures have emerged as a compact, low-profile alternative for next-generation aerospace and electronic system (AES) antennas. Composed of subwavelength scattering elements, they enable beamforming, multi-beam radiation, and polarization control while remaining lightweight and conformal—ideal for UAVs, satellites, and airborne radar. Recent studies have demonstrated the strong potential of multibeam metasurfaces in applications such as satellite communications, radar imaging, adaptive surveillance, and secure wireless links [4], [5], [6]. Owing to their single- and dual-polarization multibeam capabilities, such MTS configurations are also well suited for satellite/defense platforms, distributed 5G/6G networks, vehicular radar, wireless power transfer, and simultaneous multi-directional coverage/tracking. A conceptual illustration of multi-polarized multibeam HMS along with representative application scenarios is presented in Fig. 1. Among various metasurface architectures, modulated metasurfaces (MMSs) and holographic metasurface leaky-wave antennas (HMSLWAs) have gained significant attention due to their ability to synthesize prescribed radiation patterns using a single or limited number of excitations. Modulated surfaces (MS) are electrically thin planar structures composed of subwavelength meta–unit cells (see Fig.-1), which enable precise control over electromagnetic (EM) wave propagation through engineered surface impedance (jX_s) distributions $Z_{\text{surf}}(x, y)$. Under impedance boundary condition (IBC), the induced tangential surface current $J_{\text{surf}}(x, y)$ on the metasurface relates to the local electric field $E_t(x, y)$ via:

$$\mathbf{J}_{\text{surf}}(x, y) = \hat{\mathbf{n}} \times \mathbf{H}_t(x, y) = \frac{1}{Z_{\text{surf}}(x, y)} \mathbf{E}_t(x, y), \tag{1}$$

allowing simultaneous control of amplitude, phase, and polarization of scattered fields. By spatially modulating $Z_{\text{surf}}(x, y)$ the MTS can transform an incident reference wave φ_{ref} into a desired radiated wave φ_{obj} according to the generalized holographic relation:

$$E_{\text{rad}}(x, y) \propto \mathbf{J}_{\text{surf}}(x, y)\, e^{-j\beta_0 R_f(x,y)}, \tag{2}$$

where β_0 is the free-space wavenumber and $R_f(x, y)$ is the distance from each surface element to the far-field observation point. This formulation forms the theoretical basis for beam shaping, multi-beam radiation, and orbital angular momentum (OAM) synthesis [7], [8]. For modulated metasurface (MMS), the surface impedance is often expressed as a sum of average and modulated components [3]:

$$Z_{\text{surf}}(x, y) = j\left[X_s + M(x, y)\,\text{Re}\{\phi(x, y)\}\right], \tag{3}$$

where X_s is the average reactance, $M(x, y)$ is the modulation depth, and $\phi(x, y)$ encodes the desired phase distribution for radiation. For a 2D HMS, the surface impedance is modulated within aperture area and the radiation mechanism is governed by vector momentum conservation. A spatially periodic (or quasi-periodic) modulation is characterized by:

$$\begin{aligned} \boldsymbol{\beta}_t^{mn} &= \beta_x^{mn}\hat{\mathbf{x}} + \beta_y^{mn}\hat{\mathbf{y}} \\ &= \left(\beta_x^{sw} + \frac{2\pi m}{\alpha_x}\right)\hat{\mathbf{x}} + \left(\beta_y^{sw} + \frac{2\pi n}{\alpha_y}\right)\hat{\mathbf{y}} \\ &= \beta_0 \sin\theta_{m,n}\left[\hat{\mathbf{x}}\cos\varphi_{m,n} + \hat{\mathbf{y}}\sin\varphi_{m,n}\right] \end{aligned} \tag{4}$$

where β_{sw} is the in-plane surface wave (SW) vector of the excited φ_{ref}, $(m, n) \in \mathbb{Z}$ are diffraction orders, and $(\theta_{m,n}, \varphi_{m,n})$ denote the elevation and azimuth angles of radiated beam. Additionally, polarization-insensitive MTS have been demonstrated by combining both TE and TM modes using Huygens' meta-unit cells, as reported in [9]. Multibeam, multi-feed, and low cross-polarization HMSLWAs have been achieved through surface wave superposition techniques, as presented in [10], [11], [12], [13], [14] and [15]. A single-polarized multi-beam transmit array metasurface using an external TEM-mode feed was introduced in [16]. Unlike multi-feed architectures, where the total surface current $\mathbf{J}^T_{\text{surf}}(x, y)$ is obtained as the linear superposition of multiple excitations $\mathbf{J}^p_{\text{surf}}(x, y)$, as expressed in (5), the proposed single-feed holographic formulation concentrates the available surface current into a single guided mode. Consequently, the resulting current distribution satisfies $\mathbf{J}^{\text{single}}_{\text{surf}}(x, y) \gg \mathbf{J}^p_{\text{surf}}(x, y)$, $p = 1, 2, \ldots, N_f$. This concentration of surface current leads to improved aperture efficiency (A.E.), reduced feed-network complexity, and enhanced scalability of the overall metasurface antenna architecture. These characteristics are particularly advantageous for AES, including mobile radar, satellite payloads, and multiuser communication platforms, where robustness and SWaP efficiency are paramount.

$$\mathbf{J}^T_{\text{surf}}(x, y) = \sum_{p=1}^{P} \mathbf{J}^p_{\text{surf}}(x, y) \tag{5}$$

Recent literature reports that both single-feed [17], [18] and multi-feed [8], [19], [20], [21], [22] metasurface (MTS) topologies enable multibeam, single- and multi-polarized radiation, making them suitable for applications such as satellite communications, 5G/6G networks, and radar systems, where simultaneous coverage of multiple spatial directions is required. However, multi-feed configurations generally involve complex feeding networks, whereas single-feed multibeam generation provides a more compact and

low-complexity alternative to conventional phased-array [23], [24] and reflector-based [25], [26] solutions. Notably, several multibeam approaches, such as [10], [17], and [18], rely on the superposition principle, which often leads to a reduction in gain and aperture efficiency (A.E.). In contrast, this work investigates an alternative MTS topology that demonstrates improved gain performance. Although multifunctional HMS have been extensively studied for beamforming and polarization control, prior works [8], [17], [18], [19], [20], [21], [27], [28] largely focus on physical-layer design, without explicitly addressing multiuser interactions or mobility.From a system-level viewpoint, the far-field radiation pattern produced by a multi-beam HMS inherently defines the spatial filtering experienced by different users. However, a rigorous framework linking the aperture-field formulation to multiuser operation with U users has yet to be established for HMS-based transmitters. In particular, the combined effects of beam coupling, polarization leakage, and user mobility on inter-user interference have not been systematically investigated within a unified electromagnetic–system co-design framework. The key contributions of this work are as follows:

- Development of a generalized vectorial aperture-field framework for single-feed MTS antennas enabling multi-beam and multi-polarized radiation, consistent with GSTC/modulation theory and providing a unified approach to Z_{surf} synthesis with practical design applicability.
- Comprehensive analysis and comparative evaluation of dual-impedance modulation schemes, supported by full-wave electromagnetic modeling and experimental validation, providing deeper insight into HMS antenna performance characteristics.
- Introduction of an orthogonally segmented modulation strategy as an alternative to conventional full-aperture multiplexing, demonstrating improved realized gain and aperture efficiency (AE).
- Establishment of a mobility-aware multiuser framework that links aperture-field distributions to user-specific interference metrics (e.g., SIR_u, SINR_u), enabling systematic optimization of beam allocation, aperture modulation, and polarization control.

It is well recognized that the transformation from equivalent surface currents to aperture fields and far-field radiation is a classical problem, extensively studied for leaky-wave and holographic metasurfaces (MTS), particularly within generalized sheet-transition condition (GSTC)- and modulation-based frameworks [1], [4], [8], [12], [21]. In these approaches, radiation is governed by surface-impedance modulation, where the leakage parameters (α, β) are locally determined via momentum matching between the surface wave and radiated space harmonics.

In this work, rather than redefining this foundation, we extend it to a generalized aperture-field formulation that remains consistent with GSTC/modulation physics while operating at the field level. The proposed model incorporates a vectorial, polarization-aware representation with multi-harmonic superposition, enabling simultaneous synthesis of multiple beams with distinct polarization states from a single-feed excitation, and supporting practical simulation and measurement scenarios.

II. THEORETICAL APERTURE-FIELD ANALYSIS

As illustrated in Fig. 1, the proposed modulated metasurface (MTS) consists of a nonuniform two-dimensional arrangement of subwavelength meta-unit elements distributed over the x–y plane and located at $z = 0$. Referring to (3), the electric-field distribution over the MTS aperture can be expressed as [3]

$$E_a(x,y) = E_{sw}(x,y)\, M(x,y)\, P(x,y), \tag{6}$$

where $E_{sw}(x,y)$ denotes the surface-wave (SW) field launched by the source feed, $M(x,y)$ represents the impedance modulation function, and $P(x,y)$ is the aperture indicator (window) function, defined as $P = 1$ inside the aperture area A and $P = 0$ outside it.

In the far-field region, the radiated electric field in the direction (θ,φ) can be written as

$$\begin{aligned} E_\infty(\theta,\phi) &\propto \mathcal{F}\{E_a\}(\beta_x,\beta_y) \\ &= \int\int_A E_a(x,y)\, e^{-j(\hat{\mathbf{x}}\beta_x+\hat{\mathbf{y}}\beta_y)}\, dx\, dy, \end{aligned} \tag{7}$$

where $\mathcal{F}\{\cdot\}$ denotes the two-dimensional Fourier transform.

For uniform modulation, i.e., $M(x,y) = M_0$, the aperture field simplifies to $E_a = M_0 E_{sw} P$, and the corresponding far-field expression can be written in terms of an effective Fourier transformation, expressed as,

$$\begin{aligned} \mathcal{F}\{E_a\} &= \mathcal{F}\{M_0\} * \mathcal{F}\{E_{sw}\} * \mathcal{F}\{P\} \\ &= \left[2\pi a \frac{\mathbf{J}_1(a\beta_\rho)}{\beta_\rho}\right]^2 M_0\, \mathcal{F}\{E_{sw}\}, \end{aligned} \tag{8}$$

where * denotes convolution and $J_1(\cdot)$ is the first-order Bessel function of the first kind. In (8), instead of multiplication, convolution is used by assuming M_0 is constant, $\mathcal{F}\{M_0\} = M_0\delta(\beta)$, and the convolution with the delta function reduces to multiplication. Therefore,

$$\mathcal{F}\{E_a\} = M_0\, \mathcal{F}\{E_{sw}\} * \mathcal{F}\{P\}. \tag{9}$$

As demonstrated, $\mathcal{F}\{E_{sw}\}$ is slowly varying compared to $\mathcal{F}\{P\}$, the convolution can be approximated as a product:

$$\mathcal{F}\{E_a\} \approx M_0 \left[2\pi a \frac{J_1(a\beta_\rho)}{\beta_\rho}\right]^2 \mathcal{F}\{E_{sw}\}. \tag{10}$$

Further, the Fourier equivalence of the radially propagating surface wave is obtained by assuming $E_{sw}(x,y) \to E_{sw}(\rho)$, yielding

$$\begin{aligned} \mathcal{F}\{E_{sw}\}(k_\rho) &= \int_0^\infty \int_0^{2\pi} E_{sw}(\rho)\, e^{-j\beta_\rho \rho \cos(\psi-\psi_k)}\, \rho\, d\psi\, d\rho \\ &= 2\pi \int_0^\infty E_{sw}(\rho)\, J_0(\beta_\rho \rho)\, \rho\, d\rho, \end{aligned} \tag{11}$$

$$\textit{Note:} \left[\int_0^{2\pi} e^{-j\beta_\rho \rho \cos(\psi-\psi_k)}\, d\psi = 2\pi J_0(\beta_\rho \rho)\right]$$

The surface-wave field $E_{sw}(\rho)$ is assumed to follow a slowly decaying exponential envelope and is expressed as $E_{sw}(\rho) = A(\rho)\, e^{-j\beta_{sw}\rho} = E_0\, e^{-(\alpha+j\beta_{sw})\rho}$. For the proposed MTS design, a rectangular aperture with physical dimensions $-L_x/2 \le x \le L_x/2$ and $-L_y/2 \le y \le L_y/2$ is considered. Under these assumptions, the far-field Fourier-equivalent electric field can be expressed as

$$\begin{aligned} E_\infty(\beta_x,\beta_y) \propto & \left(\frac{4\sin\left(\frac{\beta_x L_x}{2}\right)\sin\left(\frac{\beta_y L_y}{2}\right)}{\beta_x\beta_y}\right)^2 M_0 \\ & \times \int_{-L_y/2}^{L_y/2}\int_{-L_x/2}^{L_x/2} E_0\, e^{-(\alpha+j\beta_{sw})\sqrt{x^2+y^2}} \\ & \times e^{-j(\hat{\mathbf{x}}\beta_x+\hat{\mathbf{y}}\beta_y)}\, dx\ dy \\ = & L_x^2 L_y^2 M_0 E_0\, \mathrm{sinc}^2\left(\frac{\beta_x L_x}{2}\right)\mathrm{sinc}^2\left(\frac{\beta_y L_y}{2}\right) \\ & \times \int_0^\infty e^{-(\alpha+j\beta_{sw})\rho}\mathbf{J}_0(\beta_\rho\rho)\,\rho\, d\rho, \end{aligned} \tag{12}$$

The above aperture-field formulation corresponds to a single center-fed, single linearly polarized broadside beam $(\theta_0,\varphi_0) = (0^\circ, 0^\circ)$ generated by a square MTS aperture. Since this work focuses on a multibeam, multi-polarized MTS framework, the following subsection extends the field analysis to the generalized case.

A. MULTI-POLARIZED MULTIBEAM APERTURE-FIELD ANALYSIS

In this article, we propose two distinct single-feed, multibeam multi-polarized MTS apertures with dual and multi azimuth-planar radiation. As proposed, MMS design-1 exhibits both linear and circular polarization while design-2 radiated dual linearly polarized beams. To ensure multi-polarization choice, we introduce:

$$\hat{\mathbf{e}}_p = \begin{cases} \arg\left(\frac{1}{\sqrt{2}}(\hat{\mathbf{x}} \pm j\hat{\mathbf{y}})\right): & \text{LHCP or RHCP} \\ \arg\hat{\mathbf{x}}: & \text{HP} \\ \arg(\pm j\hat{\mathbf{y}}): & \text{VP} \end{cases} \tag{13}$$

into (12) and re-write as:

$$\begin{aligned} E_\infty(\beta_x,\beta_y) \propto & \tilde{C}\int_{-L_y/2}^{L_y/2}\int_{-L_x/2}^{L_x/2} E_0\, e^{-(\alpha+j\beta_{sw})\sqrt{x^2+y^2}} \\ & \times \sum_{p=1}^{P} \hat{\mathbf{e}}_p \cdot e^{-j\beta_0\sin\theta_p(\hat{\mathbf{x}}\cos\varphi_p+\hat{\mathbf{y}}\sin\varphi_p)}\, dx\ dy \end{aligned} \tag{14}$$

where,

$$\tilde{C} = \left(\frac{4\sin\left(\frac{\beta_x L_x}{2}\right)\sin\left(\frac{\beta_y L_y}{2}\right)}{\beta_x\beta_y}\right)^2 * M_0. \tag{15}$$

Following the analytical formulation in 14, the synthesized aperture-field distribution is illustrated in Fig. 2. Four distinct high-intensity surface-current regions ($J_{\theta,\varphi}$, Fig. 2(a)) are observed within the square MTS aperture, confirming accurate multibeam excitation via surface-impedance–driven

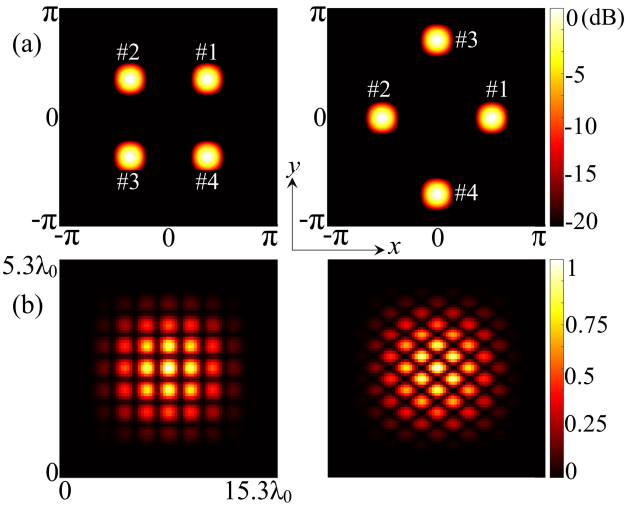


FIGURE 2. MATLAB©-extracted results showing (a) antenna directivity patterns for single point-source excitation with aperture multiplexed four-beam operation, and (b) $|J_{\theta,\varphi}|$ amplitude distributions for MMS designs 2 and 1 respectively.

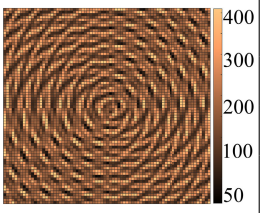
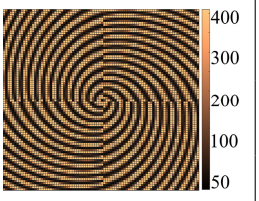
momentum matching. The surrounding interference pattern arises from the controlled superposition of modulated surface-wave harmonics, consistent with theoretical predictions. The symmetry and uniform intensity of the dominant lobes indicate effective polarization decoupling and balanced power allocation, validating the proposed multipolarized MTS framework for spatially multiplexed radiation. In comparison, MMS design-2 exhibits stronger spatial localization, with energy confined to discrete periodic regions across the aperture. Conversely, MMS design-1 shows a smoother and more continuous field distribution, with energy concentrated near the aperture center and gradually tapering toward the edges. As a result, design-2 achieves a more confined main beam with improved beam shaping and reduced sidelobe levels, whereas design 1 produces broader beams with relatively higher sidelobe radiation.

B. SURFACE IMPEDANCE (Z_{SURF}) FORMULATIONS FOR MTS DESIGNS

As illustrated in Fig. 1, the MTS configuration is governed by a prescribed surface-impedance distribution of the meta–unit cells, determined by the source-feed localization, polarization state, and desired radiation characteristics. Following the optical holographic principle, the phase term $\phi(x,y)$ appearing in (3) and (14) is synthesized through the interaction between the reference wave phase φ^*_{ref} and the object wave phase φ_{obj}, corresponding to the surface-wave excitation and the desired far-field wave vector, respectively. Furthermore, as indicated in (14), an additional phase function ($\hat{\mathbf{e}}_p$) is incorporated to enable dual- and multi-polarized radiation. The complete set of phase functions employed to realize multi-polarized operation for MMS Designs-1 and-2 is summarized in Table- 1, along with MATLAB© visualizations of the resulting surface-impedance $Z_{\mathrm{surf}}(x,y)$ distributions over the MTS aperture.

As summarized in Table- 1, MTS design-1 exploits the full aperture area for each individually polarized beam, whereas

TABLE 1. Description of additional, reference and object wave-vectors for proposed multipolarized MTS at 25 GHz.

MTS Type	Beam Location & Polarization	φ_{ext}	φ_{obj}	φ_{ref}	Z_{surf} Visualization
Quad-beam dual azimuth-planar multipolarized MTS	$-35°, 0°$ (HP)	$e^{\pm jn\pi}, \begin{cases} 0 : y_j < 0 \\ 1 : y_j > 0 \end{cases}$	$e^{j\beta_t^{mn}(\theta_1,\varphi_1)}$	$e^{-j\beta_0 nR(x,y)}$	
	$-18°, 0°$ (LHCP)	$e^{-j\left(\tan^{-1}\frac{y_j-y_0}{x_i-x_0}+\frac{\pi}{4}\right)}$	$e^{j\beta_t^{mn}(\theta_2,\varphi_2)}$		
	$25°, 0°$ (RHCP)	$e^{j\left(\tan^{-1}\frac{y_j-y_0}{x_i-x_0}+\frac{\pi}{4}\right)}$	$e^{j\beta_t^{mn}(\theta_3,\varphi_3)}$		
	$45°, 0°$ (VP)	$e^{\pm jn\pi}, \begin{cases} 0 : x_i < 0 \\ 1 : x_i > 0 \end{cases}$	$e^{j\beta_t^{mn}(\theta_4,\varphi_4)}$		
Quad-beam quad ortho azimuth-planar multi linearly polarized MTS	$45°, 45°$ (HP)	$e^{\pm j0}$	$e^{j\beta_t^{mn}(\theta_1,\varphi_1)}$ $x_i > 0, y_j > 0$	$e^{-j\beta_0 nR(x,y)}$	
	$-18°, 0°$ (LHCP)	$e^{\pm j\pi}$	$e^{j\beta_t^{mn}(\theta_2,\varphi_2)}$ $x_i < 0, y_j > 0$		
	$25°, 0°$ (RHCP)	$e^{\pm j0}$	$e^{j\beta_t^{mn}(\theta_3,\varphi_3)}$ $x_i < 0, y_j < 0$		
	$45°, 0°$ (VP)	$e^{\pm j\pi}$	$e^{j\beta_t^{mn}(\theta_4,\varphi_4)}$ $x_i > 0, y_j < 0$		

MMS design-2 yields an equal segmentation of φ_{obj} across four symmetric quadrants. Consequently, four distinct φ_{obj} functions are combined using full-aperture multiplexing (see 16) to synthesize the desired $Z_{\text{surf}}(x, y)$ matrix for MMS design-1. In contrast, a discretized symmetric quadrant-based multiplexing scheme (see 17) is employed for MMS design-2. The corresponding design procedures and full-wave electromagnetic analyses, followed by CATF measurements, are presented in the subsequent sections.

$$Z_{\text{surf}}^{\text{MMS1}}(x,y) = jX_s\left[1 + M_{i,j}\text{Re}\left(\frac{1}{4}\sum_{p=1}^{P=4}\varphi_{ext}\,\varphi_{ref}^{*}\,\varphi_{obj}\right)\right] \tag{16}$$

$$Z_{\text{surf}}^{\text{MMS2}}(x,y) = jX_s\left[1 + M_{i,j}\,\text{Re}\left(\varphi_{\text{ext}}\,\varphi_{\text{ref}}^{*}\,\varphi_{\text{obj}}(\theta_k,\varphi_k)\right)\right]$$
$$\begin{cases} k=1 & : x_i > 0,\ y_j > 0, \\ k=2 & : x_i < 0,\ y_j > 0, \\ k=3 & : x_i < 0,\ y_j < 0, \\ k=4 & : x_i > 0,\ y_j < 0. \end{cases} \tag{17}$$

III. UNIT-CELL AND MTS MODELLING

A detailed flowchart is presented in [17], which describes a clear overview of the design and optimization process. The overall workflow involves the use of MATLAB©, Python©, and Ansys HFSS© in a sequential manner for numerical modeling and EM simulation.

As illustrated in Fig. 3, a grounded, dielectric-layered, square-patch scalar metasurface (MTS) unit cell with sub-wavelength periodicity ($L_g = 0.3\lambda_0$) operating at $f_0 = 25$ GHz is adopted for the proposed MTS modeling. To enable enhanced control of the leaky-wave (LW) response (i.e. β_t^{sw}), a thin, low-loss dielectric substrate, Rogers RT/duroid 5880 ($\epsilon_r = 2.2$, $\tan\delta = 0.0009$), is employed.

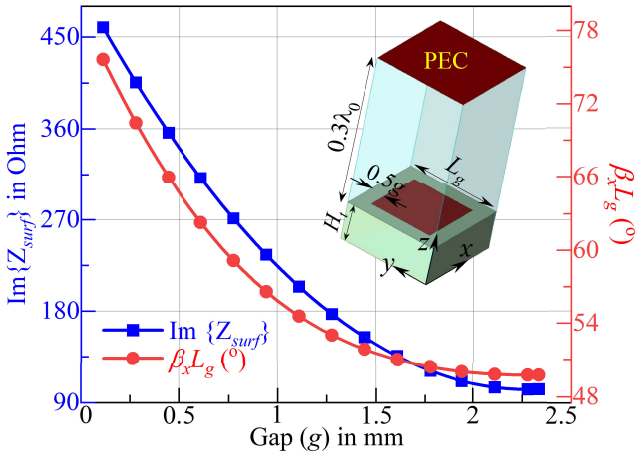


FIGURE 3. Ansys HFSS©-extracted dispersive phase response ($\beta_x L_g$) and imaginary surface impedance (Im(Z_{surf})), as functions of the unit-cell parameter g at 25GHz. The gap size g varies from 0.3 to 2.3 mm, with a fixed unit-cell periodicity L_g = 3.6 mm. Im(Z_{surf}) and $\beta_x L_g$ plot is coloured with blue and red respectively. Dimensions (in mm): H_t = 1.57.

Furthermore, a wide variation of the gap parameter g is utilized to effectively modulate the metasurface aperture characteristics. An eigenmode simulation is performed in Ansys HFSS© to characterize the dispersive behavior at 25 GHz. A highly refined mesh (i.e. 0.0001%) is employed for the dispersion analysis under periodic boundary conditions (PBC). As shown in Fig. 3, a wide dispersive phase variation ($\beta_x L_g$) is achieved, spanning from 48° to 80°. Correspondingly, using (18), the imaginary part of the surface impedance, Im(Z_{surf}), varies from 92 Ω to 472 Ω at the operating frequency.

$$Z_{\text{surf}} = jZ_0\sqrt{1-\left(\frac{\beta_x c}{2\pi f_0}\right)^2}. \tag{18}$$

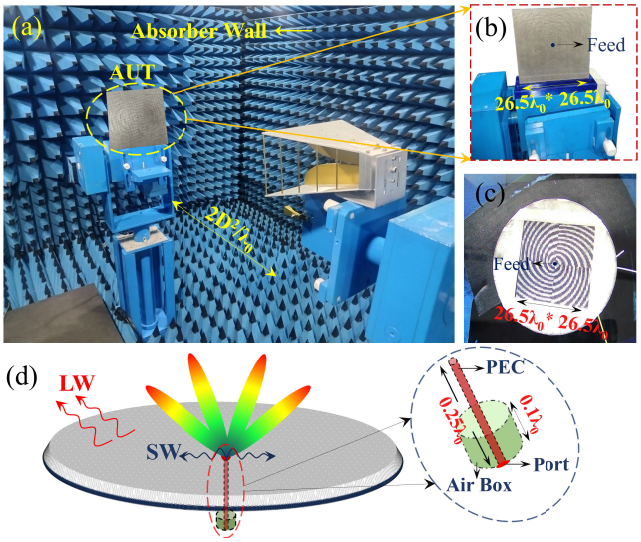


FIGURE 4. (a) Complete far-field measurement setup employing a compact antenna test facility (CATF); (b) fabricated prototype of the (b) MTS design 1, and (c) MTS design 2; and (d) detailed schematic of the surface-wave (SW) launcher (i.e., monopole feeder).

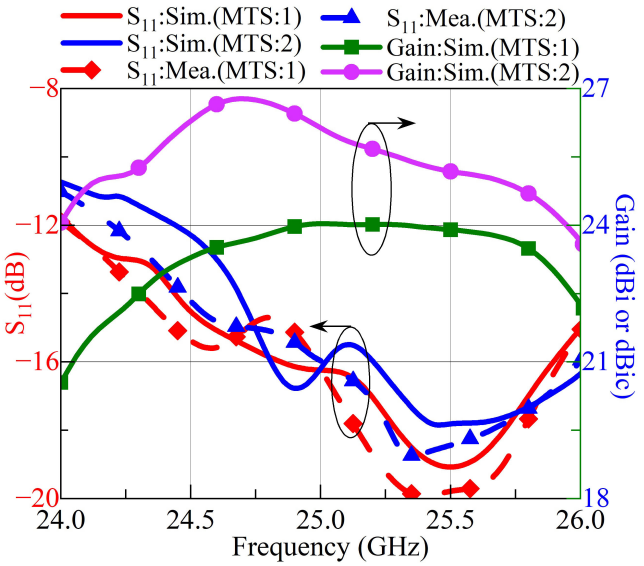


FIGURE 5. Simulated and measured S_{11} (dB) versus frequency (GHz) for MTS Designs 1 and 2. Additionally, peak gain (g_{max}) versus frequency (GHz) is presented for both designs. (*Note: The average gain curve is included, as all beams exhibit nearly identical peak gain values).

After extracting the Z_{surf} behavior of the proposed unit cell, the analysis is extended to metasurface (MTS) modeling based on the corresponding radiation characteristics. As discussed in section-(II-B), the full-aperture and quadrant-multiplexed Z_{surf} relationships, derived in (16) and (17), are responsible for the realization of MMS designs 1 and 2, respectively. Furthermore, to accurately map the calculated surface impedance Z_{surf} of the metasurface (MTS) onto the unit-cell grid matrix, thereby enabling the desired beam characteristics at 25 GHz, a third-order polynomial fitting relationship is employed. This fitting plays a crucial role in ensuring an accurate correspondence between the required impedance distribution and the geometrical parameter of the unit cell. The relationship can be expressed as

$$Z_{\text{surf}}^{\text{fit}} = -19.56\ g^3 + 126.26\ g^2 - 267.69\ g + 309.55. \quad (19)$$

Both MTS designs comprise $88 \times 88 = 7744$ meta unit cells, resulting in an overall aperture size of $26.5\lambda_0 \times 26.5\lambda_0$ at 25 GHz. Specifically, the surface impedance parameters, namely the surface reactance $X_s = 165.43$ and a constant modulation index, $M = 0.45$ is considered to achieve accurate beam positioning with the desired polarization state. Furthermore, numerical interpolation is employed to extract the equivalent unit-cell matrix corresponding to the calculated Z_{surf} grid. Both MTS designs are locally excited by a surface-mounted $\lambda_0/4$ monopole, as illustrated in Fig. 4(d), which launches a radially propagating TM_{01} surface wave with exponential amplitude decay across the MTS aperture.

IV. EM SIMULATION, MEASUREMENT, AND DISCUSSION

The proposed modulation schemes are validated via FEM simulations and CATF measurements. A complete measurement setup is shown in Fig. 4(a), where the MTS antennas are positioned inside an anechoic chamber and separated by a far-field distance from a K-band transmitting horn antenna. The fabricated prototypes of MTS Designs 1 and 2 are presented in Fig. 4(b) and Fig. 4(c), respectively. As summarized in Table- 1, design-1 generates multi-polarized quad beams at $\varphi = 0°, 90°$, while design-2 steers quad beams toward $\varphi = 45°, 135°, 225°, 315°$ with dual linear polarization.

As shown in Fig. 5, both MTS designs demonstrate good impedance matching across the 24–26 GHz band, corresponding to a 2 GHz (8.33%) impedance bandwidth, with S_{11} remaining below −10 dB. A clear difference in gain performance between MTS designs-1 and-2 is also observed in Fig. 5. MTS design 1 employs full-aperture-based φ_{obj} multiplexing, resulting in a peak gain of $g_{\max} = 23.87$ dBi. In contrast, MTS design-2 utilizes orthogonal quadrant-sectored independent multiplexing, achieving a higher peak gain of $g_{\max} = 27$ dBi, which is approximately 3 dB greater than that of design-1. This gain enhancement has a significant impact on the aperture efficiency (A.E.) and beam correlation characteristics of the proposed MTS designs. To comparatively evaluate the radiation performance of both the proposed MTS designs, the realized gain patterns over the elevation angle (θ_z) at the specified azimuth angles (φ_z) are presented in Figs. 6 & 7, respectively.

As demonstrated earlier, MMS design-1 is realized using full-aperture controlled φ_{obj} multiplexing. It produces right- and left-hand circularly polarized radiation directed towards (−20°, 0°) and (20°, 0°), respectively (see Fig. 6(a)). In addition, horizontally and vertically polarized linearly polarized beams are steered towards (−20°, 90°) and (20°, 90°), respectively (see Fig. 6(b)). Figs. 6(a) and (b) show that each circularly and linearly polarized beam achieves a peak gain ($g_{\max}$) > 23.92 dBi, with a sidelobe level (SLL) < −26.43 dB and cross-polarization discrimination (XPD) > 21.35 dB at 24.5 GHz. A similar beam-pointing characteristic and highly

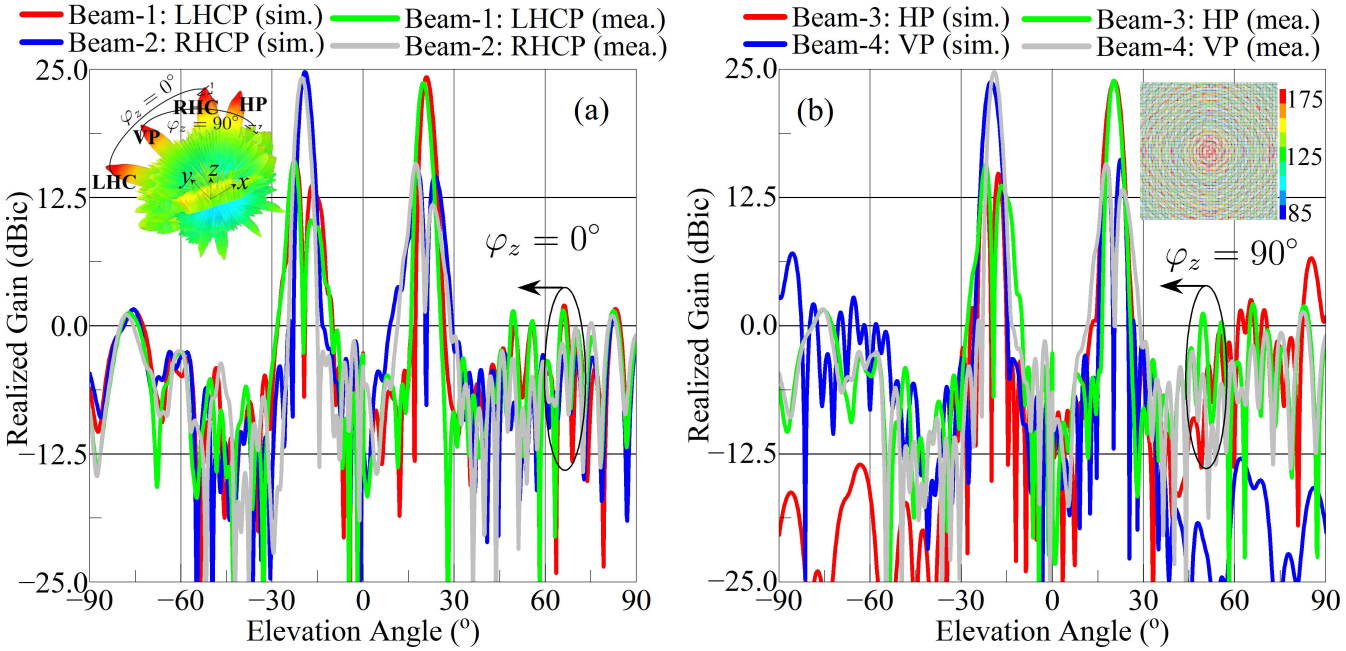


FIGURE 6. Simulated and measured realized gain patterns of the proposed MTS design 1: (a) RHCP and LHCP beams steered toward $(-20°, 0°)$ and $(20°, 0°)$, respectively; and (b) horizontally and vertically polarized linear radiation directed toward $(-20°, 90°)$ and $(20°, 90°)$, respectively. Additionally, the corresponding 3D radiation patterns and surface current (J_{surf}) distributions are presented.

TABLE 2. Comparative analysis of the proposed MTS designs in terms of beam performance metrics.

MTS \ Param.	Beam Positions (θ_z, φ_z)		Pol.		g_{max} (dBi)		SLL(dB)		AR(dB)		XPD & HPBW (dB & °)	
	sim	meas	sim	meas	sim	meas	sim	meas	sim	meas	sim	meas
Design # 1: Quad-beam dual-planar multi-polarized MTS	$20°, 0°$	$21°, 0°$	LHC	LHC	23.6	23.5	-28.25	-27.12	1.2	1.3	29, 3.5°	22, 3.6°
	$-20°, 0°$	$-19.5°, 0°$	RHC	RHC	24.2	23.8	-24.21	-24.23	1.35	1.62	23, 5.5°	24, 5.6°
	$20°, 90°$	$19.5°, 90°$	HP	HP	23.4	23.3	-24.5	-23.9	–	–	32, 5.4°	25, 5.3°
	$-20°, 90°$	$-20.5°, 90°$	VP	VP	24.5	23.9	-26.24	-24.14	–	–	36, 4.9°	28, 4.8°
Design # 2 : Quad-beam quad ortho-planar multi-LP MMS	$20°, 45°$	$20.2°, 45°$	VP	VP	26.8	25.9	-24.3	-26.2	–		30, 4.6°	26, 5.3°
	$20°, 135°$	$20.5°, 135°$	HP	HP	27	26.1	-32.1	-31.6	–		34, 4.3°	26, 5.1°
	$20°, 225°$	$20.2°, 225°$	VP	VP	26.5	25.7	-26.4	-26.3	–		37, 4.7°	28, 5.8°
	$20°, 315°$	$20.5°, 315°$	HP	HP	26.6	25.7	-19.8	-18.6	–		41, 5.1°	32, 5.9°

∗Note :Modulus values of XPD is considered.

directive radiation behavior are observed in the 3D radiation pattern embedded in Fig. 6(a). Furthermore, as illustrated in Fig. 5, MTS design-1 maintains a peak gain > 21 dBi over the entire 3 dB operating bandwidth, spanning 24–26 GHz. The stable peak gain around the desired operating frequency (i.e., 25 GHz), along with dual orthogonal azimuthal beam orientations, validates the effectiveness of the proposed design. Table 1 demonstrates the significant influence of the proposed Taylor-assisted tapering on SLL suppression for each multi-polarized beam, achieving an on-average SLL separation > 26, dB.

In contrast, Fig. 5 demonstrates that MMS design 2 achieves an approximately 3 dB higher peak gain compared to design 1. According to the design specifications, MMS design 2 adopts an equi-symmetric four-quadrant segmented quad-beam architecture, in which the beams are steered toward four orthogonal azimuthal directions (i.e., φ_z = $45°, 135°, 225°, 315°$), while preserving a constant elevation angle of $\theta_z = 20°$. In this configuration, each quadrant operates as an independent radiating segment responsible for a specific beam direction. This segmented architecture enables improved aperture utilization, resulting in an approximate 3 dB enhancement in peak gain and overall aperture efficiency for the proposed MTS design. Fig. 7 depicts the simulated and measured co- and cross-polar radiation, oriented at $\varphi_z = 45°, 135°$. Considering the proposed beam positions, a mirror symmetric radiation characteristics has been observed for the following pairs of azimuth planes: $\varphi_z = \{(45°, 225°), (135°, 315°)\}$.

Fig. 7 illustrates the simulated and measured realized gain patterns of the proposed MTS design-2 for dual linearly polarized beam pairs. In Fig. 7(a), for $\varphi_z = 45°$, the horizontally polarized (HP) beam-1 exhibits a g_{max} of 26.8dBi at $\theta \approx +20°$, while its mirror-symmetric counterpart

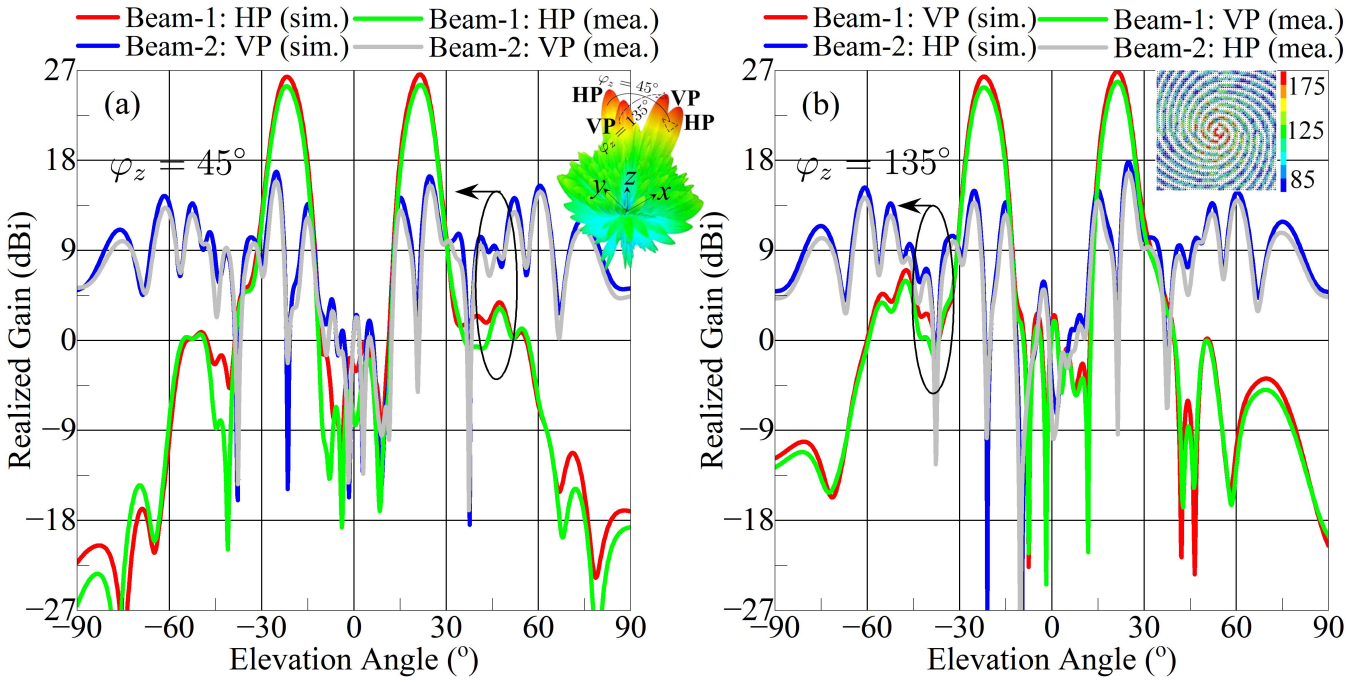


FIGURE 7. Simulated and measured realized gain patterns of the proposed MTS design 2: (a) horizontally polarized linear radiation directed toward $(20°, 45°)$, together with its mirror-symmetric beam at $(-20°, 45°)$ (originally $(20°, 225°)$); and (b) vertically polarized linear radiation directed toward $(20°, 135°)$, along with its mirror-symmetric beam at $(-20°, 135°)$ (originally $(20°, 315°)$). The corresponding 3D radiation patterns and surface current (J_{surf}) distributions are also presented. (Note: Since the $\varphi_z = 45°, 225°$ and $\varphi_z = 135°, 315°$ planes exhibit mirror symmetry, each 2D azimuth cut contains two mirror-symmetric beams within a single plane).

appears at $\theta \approx -20°$ with nearly identical magnitude. The measured peak gain closely follows the simulated result with a deviation of less than 0.5 dB. In Fig. 7(b), for $\varphi_z = 135°$, the VP Beam-1 achieves a g_{max} of 26.5dBi at $\theta \approx +20°$ and $-20°$, again demonstrating strong mirror symmetry. The simulated and measured patterns exhibit excellent agreement in beam direction and amplitude, confirming accurate phase compensation across the aperture. The corresponding 3D radiation patterns and surface current (J_{surf}) distributions further validate the proper excitation of the intended linear polarization states and symmetric aperture field distribution.

Compared to Fig. 7, Fig. 6 demonstrates polarization-agile beam synthesis including circularly polarized (CP) and additional linear polarization (LP) states. In Fig. 6(a), the LHCP and RHCP beams achieve peak realized gains of 24–25 dBic at $\theta \approx \pm 20°$ in the $\varphi_z = 0°$ plane, which is about 2–3 dB lower than the peak linear-polarized gain observed in Fig. 7 (~27 dBi). However, Fig. 6 provides dual-sense CP functionality with good symmetry and comparable gain balance between LHCP and RHCP beams, which doesn't suit with the design strategy of MTS design 2. Furthermore, Fig. 6(b) presents additional HP and VP beams in the $\varphi_z = 90°$ plane with peak gains around 23–25 dBi, slightly lower than the maximum gain of Fig. 7 but offering enhanced polarization diversity and beam multiplicity. Therefore, design-2 outperforms design-1 in terms of maximum achievable linear-polarized peak gain (by 2–3 dB) and slightly better polarization discrimination. In contrast, as shown in Fig. 6 and Fig. 7, design-1 outperforms design-2 in multi functionality,enabling circular polarization generation and additional orthogonal beam states with comparable beam steering accuracy and stable gain performance. Overall, Fig. 7 emphasizes higher peak gain with better aperture efficiency (A.E) with linear beam performance, whereas Fig. 6 prioritizes polarization multiplexing and multi-mode radiation capability with marginal gain trade-off. Additionally, an extensive detailing for necessary antenna parameters of the proposed MTS designs are listed in Tables 2 and 3 respectively. Some of the key parameters where MTS design-2 is out performed by design-1 are listed as follows:

- MTS design-2 achieves the highest peak gain (= 27 dBi) and aperture efficiency (5.75%), representing an improvement of > 170% over design-1.
- MTS design-2 exhibits significantly reduced SLL (27.2 – 28.9) dB, corresponding to an enhancement of approximately 58 – 74% compared to the other designs.
- An increase of up to 18% in HPBW for design-2 indicates improved angular coverage and enhanced broadband performance.
- MTS design-2 realizes ortho-planar quad-beam radiation, enabling full-quadrant spatial coverage.
- The pure linear (HP/VP) polarization of design-2 ensures distinct beam isolation, removes axial-ratio constraints, and preserves sufficient cross-polarization discrimination (XPD).

Table- 4 benchmarks the proposed MTS designs against existing MTS-based LWAs, demonstrating that the proposed approaches achieve markedly enhanced aperture efficiency and axial-ratio bandwidth with strong polarization diversity

TABLE 3. Comparison of IBW, ARBW, and 3-dB GBW for the proposed MMS designs.

MTS Type	Beam Position $\{\theta_z, \varphi_z\}$		IBW (sim & mea)	ARBW		3-dB GBW	
	sim	meas		vs freq (GHz) sim & mea	vs deg (°) sim & mea	vs freq (GHz) sim & mea	vs deg (°) sim & mea
Design #1	$20°, 0°$	$21°, 0°$	1.8 GHz (24.2 – 26) 8.12%	2 GHz (24 – 26) 8.33%	6.1° (17.8 – 24.9)	1.7 GHz (24.3 – 26) 8.09%	4.7 & 4.9
	$-20°, 0°$	$-19.5°, 0°$					5.5 & 5.6
	$20°, 90°$	$19.5°, 90°$					5.4 & 5.3
	$-20°, 90°$	$-20.5°, 90°$					4.9 & 4.8
Design #2	$20°, 45°$	$20.2°, 45°$	1.95 GHz (24.05 – 26) 8.32%	–	–	1.5 GHz (24.5 – 26) 7.82%	4.6 & 5.3
	$20°, 135°$	$20.5°, 135°$					4.3 & 5.1
	$20°, 225°$	$20.2°, 225°$					4.7 & 5.8
	$20°, 315°$	$20.5°, 315°$					5.1 & 5.9

∗Note :IBW- Impedance bandwidth, ARBW- axial ratio bandwidth, GBW- gain bandwidth

TABLE 4. Comparison between proposed MTS Designs & other related works.

Param. / Ref. no	f_r (GHz)	MTS Type	Phy dim. (cm×cm)	Elec dim. ($\lambda_0 \times \lambda_0$)	No. of Feed	No. of Beams	g_{max} (dBi/dBic)	Pol	A.E (%)	ARBW (%)
[8]	14.1	Tensor	40×40	18.8×18.8	7	7 (1per feed)	20	LP	8	——
[17]	25	Scalar	12.5×12.5	10.5×10.5	1	2	19.17	CP & LP	5·8	20.4
[18]	25	Tensor	10×10	8.3×8.3	1	3	10.2	LP (Dual)	8.3	——
[19]	15	Tensor	28×25	14×12.5	5	5(1per feed)	13.93	LP	1.12	——
[20]	26.2	Tensor	8.9×8.9	7.4×7.4	2	2	22.1	RHCP	23.6	3.2
[21]	24	Tensor	$\pi(12.5)^2$	$\pi(10\lambda_0)^2$	3	3	20	CP	2.53	N.A
[22]	24	Tensor	$\pi(12.5)^2$	$\pi(10\lambda_0)^2$	4	2	21	LHCP	3.19	N.A
[27]	10	Scalar	23.2×23.2	7.3×7.3	1	1	13	RHCP	5.85	4.9
[28]	10	Tensor	32.8×32.8	10.9×10.9	1	1	16	CP (Dual)	6.02	7.25
T.W	25	Scalar	31.5×31.5	26.5×26.5	1	4	**24.5**	**CP & LP**	**3.2**	**8.33**
							27	**LP (HP & VP)**	**5.75**	——

∗Note :T.W-This work, Phy.dim- physical dimension, Elec. dim-electrical dimension, Pol-polarization, A.E-aperture efficiency

in design-1, or superior gain and sidelobe suppression in design-2, while maintaining competitive performance in all other key metrics. It is observed that beam performance is strongly influenced by both the modulation strategy and the spatial distribution of beams. In particular, orthogonal quadrant segmentation combined with mutually orthogonal azimuthal beam placement significantly reduces inter-beam interference, leading to improved radiation performance compared to conventional full-aperture multiplexing approaches.

Despite the comparison of key performance metrics, both MTS designs demonstrate multi-planar radiation with multi-polarized characteristics. These features make them particularly suitable for mobility-aware multiuser modeling within an H-matrix framework, facilitating spatial- and polarization-division multiple access (SP-PDMA). A detailed characterization is provided in the subsequent section.

V. MOBILITY-AWARE MULTIUSER MODELING

In the preceding sections, the proposed MTS designs are evaluated in terms of peak gain (g_{max}), SLL, beamwidth, and polarization purity. For mobility-aware multiuser deployment, these electromagnetic metrics are translated into communication-level performance indicators. Beyond spatial beam steering, the MTS platform enables interference suppression through polarization-domain orthogonality. Hence, a unified signal-processing framework is formulated to evaluate spatial–polarization division multiple access (SP-PDMA) under user mobility.

Let's consider a downlink multi-user scenario, consisting of K independent users, served simultaneously by the proposed MTS transmitter (see Fig.-1). Considering each user is assigned a distinct spatial beam, located at a fixed angular position (θ_u, φ_u) with a polarization state of $\mathbf{P}_u$, the modified space-polarization dependent impedance relationship ($Z_{surf}(x, y)$) is expressed as:

$$Z_{surf}(x,y) = j\left[X_s + M_{i,j}\sum_{u=1}^{K}\mathrm{Re}\left(\mathbf{P}_u e^{-jk_0\hat{\mathbf{r}}_k\mathbf{r}}\right)\right], \tag{20}$$

where $\hat{\mathbf{r}}_k$ denotes the unit vector pointing toward the desired beam direction (θ_u, φ_u), and $\mathbf{P}_u$ represents the corresponding polarization vector associated with the u-th beam. As discussed previously, MTS design-1 supports multi-polarized radiation characteristics, namely LHCP, RHCP, horizontally polarized (HP), and vertically polarized (VP) beams. In

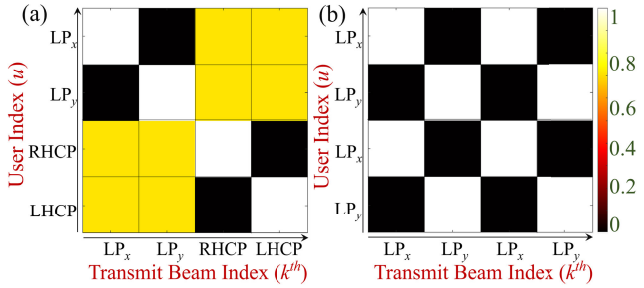


FIGURE 8. Polarization mismatch matrices for the proposed MTS designs (a) Design 1 and (b) Design 2, evaluated for four independent users employing orthogonal polarization states (LP_x, LP_y, LHCP, RHCP).

contrast, design-2 produces a pair of linearly polarized beams distributed over orthogonal azimuth planes. Accordingly, the polarization vectors, followed by Jones vector formulation, can be numerically formulated as follows:

$$\mathbf{P}_u = \begin{cases} \begin{bmatrix} 1 & 0 \end{bmatrix}^T : \mathrm{HP}(\mathrm{LP}_x) \\ \begin{bmatrix} 0 & 1 \end{bmatrix}^T : \mathrm{VP}(\mathrm{LP}_y) \\ \frac{1}{\sqrt{2}} \begin{bmatrix} 1 & -j \end{bmatrix}^T : \mathrm{RHCP} \\ \frac{1}{\sqrt{2}} \begin{bmatrix} 1 & j \end{bmatrix}^T : \mathrm{LHCP} \end{cases} \tag{21}$$

In this proposed scenario, each MTS design exhibit multi-polarized radiation to fixed direction. The polarization coupling between k^{th} transmit beam and user u is defined as: $\eta_{u,k} = \mathbf{P}_u^H \mathbf{P}_k$. Here, $\mathbf{P}_u^H$ indicates the complex conjugated transform, while resulting polarization mismatch matrix is expressed as:

$$\mathbf{P} = \left(|\mathbf{P}_u^H \mathbf{P}_k| \right)_{u,k} : |\eta_{u,k}| = \begin{cases} 1 : \mathrm{PerfectlyAlign} \\ 0 : \mathrm{OrthogonalPol.} \end{cases} \tag{22}$$

This matrix quantifies the intrinsic polarization-domain interference suppression capability of the MTS. Following proposed MTS designs, the polarization mismatch matrix is demonstrated in Fig 8.

Aligned with XPD performances for respective CP and LP beams, the polarization mismatch matrices (in Fig. 8) confirm that the proposed modulated MTS can synthesize orthogonal polarization states with high purity. The mixed linear–circular configuration provides enhanced polarization diversity at the expense of moderate cross-domain coupling, whereas the dual-linear configuration achieves near-binary polarization isolation, offering improved interference suppression under SP-PDMA operation. As considered, each independent user is characterized by a nominal angular position (θ_u, φ_u) and an associated polarization state $\mathbf{P}_u$. Under mobility, the instantaneous angular position is modeled as,

$$\theta_u(t) = \theta_u + \Delta\theta_u(t), \qquad \varphi_u(t) = \varphi_u + \Delta\varphi_u(t), \tag{23}$$

where $\Delta\theta_u(t)$ and $\Delta\varphi_u(t)$ denote random angular perturbations modeled as independent zero-mean Gaussian processes,

$$\Delta\theta_u(t),\ \Delta\varphi_u(t) \sim \mathcal{N}(0, \sigma_t^2), \tag{24}$$

with variance σ_t^2. This stochastic representation captures small-scale directional variations arising from user mobility, beam-tracking inaccuracies, or environmental disturbances. The angular misalignment directly affects the effective MTS gain perceived by the user. For analytical tractability, the far-field radiation pattern corresponding to the k^{th} steered beam is approximated using a Gaussian profile.

Accordingly, the instantaneous spatial gain experienced by user u from beam k is expressed as,

$$\gamma_{u,k}(t) = G_k(\theta_u(t), \varphi_u(t)) = e^{-\frac{(\theta_u(t)-\theta_k)^2}{2\sigma_b^2} - \frac{(\varphi_u(t)-\varphi_k)^2}{2\sigma_b^2}} \tag{25}$$

where (θ_k, φ_k) denotes the steering direction of the k^{th} beam, and σ_b controls the effective beamwidth. This formulation establishes a direct linkage between radiation-domain characteristics and the resulting system-level gain. In the next step, by incorporating both spatial gain and polarization coupling effects, the effective channel coefficient between the k^{th} transmit beam and user u can be expressed as follows:

$$h_{u,k}(t) = \sqrt{\gamma_{u,k}(t)}\, \mathbf{P}_u^H \mathbf{P}_k \,;\, \mathbf{H}_{\mathrm{PMU}} = \begin{bmatrix} h_{11} & h_{12} & \cdots \\ h_{21} & h_{22} & \cdots \\ \vdots & \vdots & \ddots \\ h_{n1} & h_{n2} & \cdots \end{bmatrix}_{(u,k)} \tag{26}$$

Finally, the received signal model for each specific user is expressed as:

$$y_u = \eta_{u,u} G_u(\theta_u, \varphi_u) s_u + \sum_{k \neq u} \eta_{u,k} G_k(\theta_u, \varphi_u) s_k + n_u. \tag{27}$$

Here, in (27), the first term indicates desired signal response while the second term demonstrates the interference and polarization mismatch between users. Additionally, the term n_u denotes the additive complex Gaussian noise at the u^{th} user terminal, modeled as $n_u \sim \mathcal{CN}(0, \sigma_n^2)$.It accounts for receiver thermal noise, RF front-end impairments, and background electromagnetic noise. This component establishes the fundamental SNR limit of the proposed MTS-based multi-beam antenna system and becomes dominant under well-aligned beam conditions where inter-user interference is minimized. Formulating $\mathbf{H}_{\mathrm{PMU}}$ matrix for the proposed MTS designs with four specific directed beams and mobile users, the polarimetric $\mathbf{H}$-matrix magnitude is formulated and shown in Fig.- 10. The $\mathbf{H}$-matrix components are captured in three distinct snapshot, like $t = 1, 100, \& 200$ and displayed separately in Fig.- 10 for the MTS designs. The $\mathbf{H}_{\mathrm{PMU}}$ matrices for Designs-1 and-2 show clear diagonal dominance at $t = 1, 100$, and 200, indicating strong beam-to-user coupling with minimal inter-beam interference. Design-1 maintains consistently high diagonal entries with negligible temporal variation, reflecting stable beam alignment. Design-2 exhibits similar behavior with slightly higher fluctuations. In all cases, the near-zero off-diagonal terms confirm effective spatial and polarization isolation.

Next, the robustness of the proposed holographic MTS transmitter under user mobility is quantified through the SNR degradation induced by beam misalignment. From an EM perspective, the far-field radiation pattern is governed by the

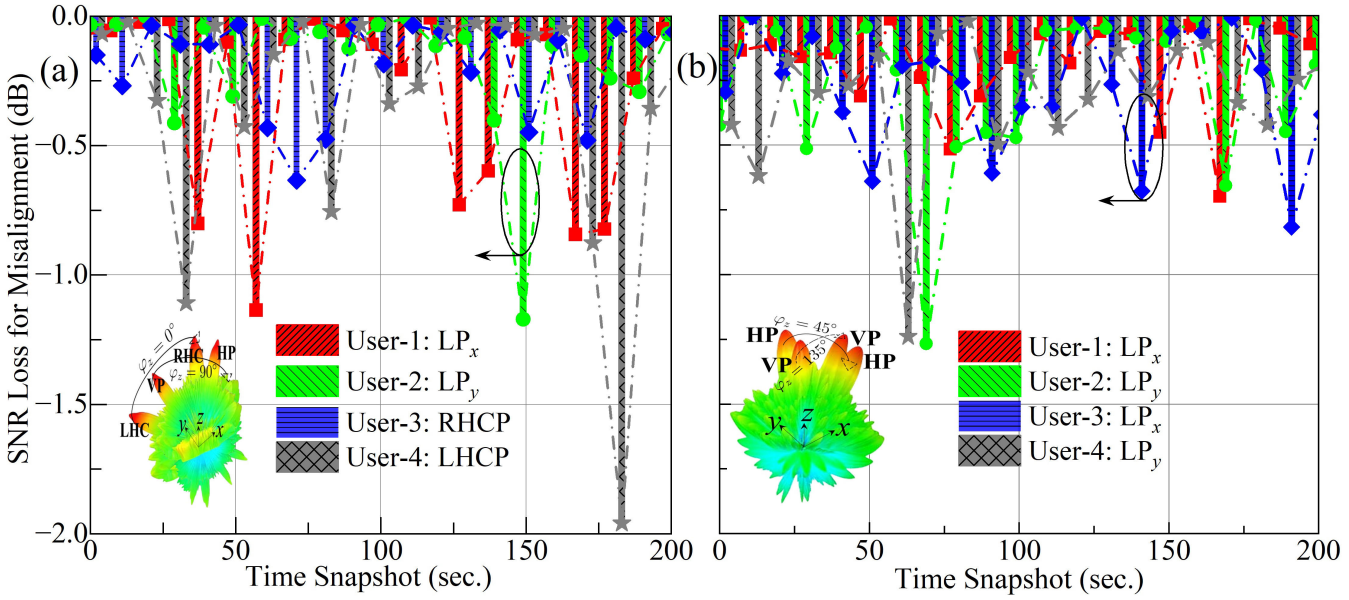


FIGURE 9. SNR degradation due to beam misalignment evaluated at discrete time snapshots $t = 10n$, where $n = 0, 1, 2, \ldots, 20$, for four distinct users employing independent polarization states, corresponding to MTS designs (a) 1 and (b) 2.

spatial Fourier transform of the synthesized aperture-field distribution in (8)–(14). The resulting pattern exhibits a Gaussian angular profile centered at the designed steering direction (θ_0, φ_0), with maximum radiation occurring when the user direction matches the engineered transverse wavenumber pair (k_{x0}, k_{y0}).

Under mobility, the user direction perturbs to $(\theta_0+\Delta\theta, \varphi_0+\Delta\varphi)$, corresponding to sampling the angular spectrum away from its peak. Owing to the exponential decay of the spectrum with transverse wavenumber deviation, the received field magnitude reduces as

$$\mathbf{F}_{\text{inst}} = \mathbf{F}_{\text{nom}} \exp\left(-\frac{\Delta\theta^2}{2\sigma_\theta^2} - \frac{\Delta\varphi^2}{2\sigma_\varphi^2}\right), \tag{28}$$

where σ_θ and σ_φ are determined by the effective aperture size via the Fourier uncertainty principle. The corresponding SNR degradation is therefore

$$\mathbf{SNR}_{\text{loss}} = 10\log_{10}\left(\frac{|\mathbf{F}_{\text{inst}}|^2}{|\mathbf{F}_{\text{nom}}|^2}\right). \tag{29}$$

Physically, this degradation reflects spectral mismatch in the spatial-frequency domain: larger apertures yield narrower beams and higher directivity, but increased sensitivity to angular perturbations, revealing an inherent robustness–directivity tradeoff.

Fig. 9 shows the SNR degradation at discrete time snapshots $t = 10n$, $n = 0, 1, \ldots, 20$, for four users under two-dimensional mobility. For both MTS Designs-1 and-2, the loss remains bounded within approximately 0 to −2 dB, confirming stable link quality for a moderate beamwidth ($\sigma_\theta = \sigma_\varphi = 6°$). Design-1 exhibits slightly larger temporal fluctuations with occasional deeper fades, whereas Design-2 demonstrates a more compact loss distribution and improved inter-user consistency, indicating enhanced robustness against

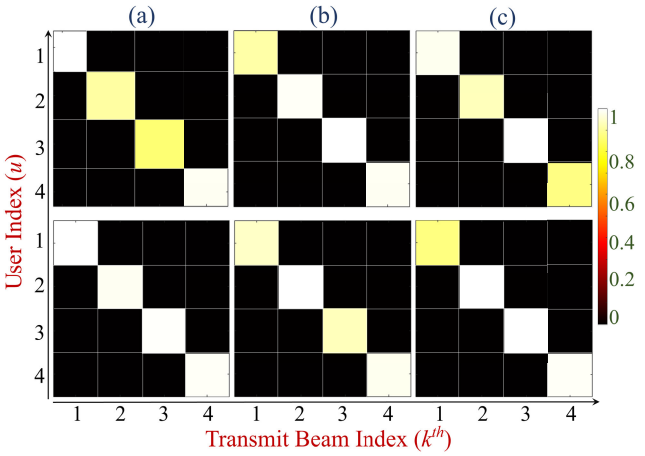


FIGURE 10. Polarimetric $\mathbf{H}_{\text{PMU}}$-matrix magnitude corresponding to MTS Designs 1 and 2 at different time instants: (a) $t = 1$, (b) $t = 100$, and (c) $t = 200$. The first and second rows represent Design 1 and Design 2, respectively.

angular misalignment. Key observations where Design-2 outperforms Design-1 in a multiuser environment are summarized as follows:

- **Reduced SNR fluctuation:** Design 2 shows smaller degradation variance and fewer deep fading events.
- **Improved user uniformity:** Design 2 maintains more consistent misalignment tolerance due to better beam symmetry and polarization isolation.

VI. CONCLUSION

This article presented a unified EM and system-level investigation of quad-beam, multi-polarized holographic metasurfaces operating at 25 GHz. An analytical aperture-field framework was demonstrated to relate scalar surface-impedance modulation with far-field beam synthesis through

spatial-frequency control. Based on this formulation, two 88×88 metasurface topologies were designed to generate prescribed multi-beam and multi-polarized radiation patterns over a $26.5\lambda_0 \times 26.5\lambda_0$ aperture. The EM analysis verified that independent beam formation and polarization selectivity arise from engineered aperture phase distributions and controlled momentum matching. The metasurface was subsequently modeled as a polarimetric H-matrix channel, enabling spatial- and polarization-division multiple access (SP-PDMA). System-level evaluations incorporating user mobility and angular misalignment quantified SNR degradation and sum-rate variations due to beam deviation. Results confirmed that multi-polarization improves user separability, mitigates inter-user interference, and enhances spectral efficiency compared to single-polarization configurations. The misalignment analysis further established a direct linkage between aperture-field perturbation and communication performance fluctuation. Overall, the proposed framework bridges large-aperture metasurface electromagnetics with multiuser MIMO modeling for high-frequency wireless communication systems.

ACKNOWLEDGMENT

The authors are highly grateful and obliged to SSPACE Laboratory, IIST, and Fortran Circuit, Electronics for the fabrication support. They are grateful to Puneet Kr. Mishra, Head, System and Integration Group, URSC, Bengaluru, India; and Haindevi Mangila, Abhinab Jha, and the entire CATF Team for their support in measurement.

REFERENCES

[1] G. Minatti et al., "Modulated metasurface antennas for space: Synthesis, analysis and realizations," *IEEE Trans. Antennas Propag.*, vol. 63, no. 4, pp. 1288–1300, Apr. 2015, doi: 10.1109/TAP.2014.2377718.

[2] I. Ghosh, S. Ghosh, S. Chatterjee, and B. Gupta, "Nonlinearly modulated scalar metasurface with circularly polarized butterfly-shaped beamforming," *IEEE Antennas Wireless Propag. Lett.*, vol. 24, pp. 756–760, 2025, doi: 10.1109/LAWP.2024.3516213.

[3] B. H. Fong, J. S. Colburn, J. J. Ottusch, J. L. Visher, and D. F. Sievenpiper, "Scalar and tensor holographic artificial impedance surfaces," *IEEE Trans. Antennas Propag.*, vol. 58, no. 10, pp. 3212–3221, Oct. 2010, doi: 10.1109/TAP.2010.2055812.

[4] M. Casaletti, M. Smierzchalski, M. Ettorre, R. Sauleau, and N. Capet, "Polarized beams using scalar metasurfaces," *IEEE Trans. Antennas Propag.*, vol. 64, no. 8, pp. 3391–3400, Aug. 2016, doi: 10.1109/TAP.2016.2570251.

[5] S. Ghosh, H. Priyadarshan, and C. Saha, "Scalar highly directive circularly polarized full{-} and half-structured holographic metasurface-based Ku-band leaky-wave antenna," *IEEE Antennas Wireless Propag. Lett.*, vol. 23, pp. 3183–3187, 2024, doi: 10.1109/LAWP.2024.3429556.

[6] H. Oraizi, A. Amini, A. Abdolali, and A. M. Karimimehr, "Design of wideband leaky-wave antenna using sinusoidally modulated impedance surface based on the holography theory," *IEEE Antennas Wireless Propag. Lett.*, vol. 17, pp. 1807–1811, 2018, doi: 10.1109/LAWP.2018.2866712.

[7] A. M. Patel and A. Grbic, "A printed leaky-wave antenna based on a sinusoidally-modulated reactance surface," *IEEE Trans. Antennas Propag.*, vol. 59, no. 6, pp. 2087–2096, Jun. 2011, doi: 10.1109/TAP.2011.2143668.

[8] Y. Wen, P.-Y. Qin, S. Maci, and Y. J. Guo, "Low-profile multibeam antenna based on modulated metasurface," *IEEE Trans. Antennas Propag.*, vol. 71, no. 8, pp. 6568–6578, Aug. 2023, doi: 10.1109/TAP.2023.3281677.

[9] K. J. Nicholson, T. C. Baum, J. E. Patniotis, and K. Ghorbani, "Discrete holographic antenna embedded in a structural composite laminate," *IEEE Antennas Wireless Propag. Lett.*, vol. 19, pp. 358–362, 2020, doi: 10.1109/LAWP.2019.2962902.

[10] S. Ghosh, E. Baladi, and C. Saha, "Single-feed multipolarized dual planar high-gain mm-wave modulated metasurface antenna," *IEEE Antennas Wireless Propag. Lett.*, vol. 24, pp. 3355–3359, 2025, doi: 10.1109/LAWP.2025.3590298.

[11] S. Ghosh and C. Saha, "Tensor surface impedance characterization of isotropic inhomogeneous metasurface backed CSRR loaded sub-6 GHz dual-band MPA," *IEEE Antennas Wireless Propag. Lett.*, vol. 23, pp. 3153–3157, 2024, doi: 10.1109/LAWP.2024.3428634.

[12] M. Mencagli, E. Martini, D. González-Ovejero, and S. Maci, "Metasurfing by transformation electromagnetics," *IEEE Antennas Wireless Propag. Lett.*, vol. 13, pp. 1767–1770, 2014, doi: 10.1109/LAWP.2014.2364981.

[13] S. Ramalingam, C. A. Balanis, C. R. Birtcher, and H. N. Shaman, "Polarization-diverse holographic metasurfaces," *IEEE Antennas Wireless Propag. Lett.*, vol. 18, pp. 264–268, 2019, doi: 10.1109/LAWP.2018.2888811.

[14] G. Liu, X. Sun, X. Chen, D. Xiong, M. Li, and M.-C. Tang, "A broadband low-profile dual-linearly polarized dipole-driven metasurface antenna," *IEEE Antennas Wireless Propag. Lett.*, vol. 19, pp. 1759–1763, 2020, doi: 10.1109/LAWP.2020.3017173.

[15] A. Li, M. Zhao, D. P. Lynch, S. Zhu, M. A. B. Abbasi, and O. Yurduseven, "Frequency-diverse reflection metasurface antenna design for computational microwave imaging," *IEEE Open J. Antennas Propag.*, vol. 5, pp. 1240–1248, 2024, doi: 10.1109/OJAP.2024.3377368.

[16] Z. H. Jiang, F. Wu, X.-W. Zhu, Q. Ren, P. L. Werner, and D. H. Werner, "Metasurface-based circularly-polarized multibeam reflect-/Transmit-arrays," in *Proc. 14th Eur. Conf. Antennas Propag. (EuCAP)*, Mar. 2020, pp. 1–3, doi: 10.23919/EuCAP48036.2020.9135820.

[17] S. Ghosh, H. Priyadarshnam, and C. Saha, "Characterization of single-feed multiple dual-polarized dual-beam scalar impedance-modulated metasurface antennas," *IEEE Trans. Antennas Propag.*, vol. 73, no. 9, pp. 6334–6343, Sep. 2025, doi: 10.1109/TAP.2025.3570514.

[18] O. Yurduseven and D. R. Smith, "Dual-polarization printed holographic multibeam metasurface antenna," *IEEE Antennas Wireless Propag. Lett.*, vol. 16, pp. 2738–2741, 2017, doi: 10.1109/LAWP.2017.2743710.

[19] Y. Wang, Q. Feng, X. Kong, H. Liu, J. Han, and L. Li, "Multifeed beam-switchable cylindrical conformal holographic metasurface antenna," *IEEE Antennas Wireless Propag. Lett.*, vol. 23, pp. 970–974, 2024, doi: 10.1109/LAWP.2023.3340682.

[20] S. Xue, Y. Shen, Z. Xu, and S. Hu, "Millimeter-wave multibeam antenna based on holographic metasurface with high aperture efficiency and low sidelobe level," *IEEE Trans. Antennas Propag.*, vol. 74, no. 1, pp. 1162–1167, Jan. 2026, doi: 10.1109/TAP.2025.3610207.

[21] M. Bodehou, E. Martini, S. Maci, I. Huynen, and C. Craeye, "Multibeam and beam scanning with modulated metasurfaces," *IEEE Trans. Antennas Propag.*, vol. 68, no. 3, pp. 1273–1281, Mar. 2020, doi: 10.1109/TAP.2019.2944554.

[22] M. Bodehou and C. Craeye, "Array surface-wave launcher for the efficient generation of shaped beam and multibeam with metasurface," *IEEE Trans. Antennas Propag.*, vol. 69, no. 12, pp. 8860–8865, Dec. 2021, doi: 10.1109/TAP.2021.3090801.

[23] T. H. Bui, S. A. Rezaeieh, K. S. Bialkowski, A. Abbosh, and C. Fumeaux, "Dual-polarized multimode hemispherical beam-scanning and null-steering antenna," *IEEE Trans. Antennas Propag.*, vol. 73, no. 10, pp. 7336–7349, Oct. 2025, doi: 10.1109/TAP.2025.3583024.

[24] Y. Fan, Y. F. Wu, L.-W. Zhao, and Y. Guo, "Pattern synthesis for beam scanning of contiguous multibeam subarrayed phased array," *IEEE Antennas Wireless Propag. Lett.*, vol. 25, pp. 891–895, 2026, doi: 10.1109/LAWP.2025.3642309.

[25] Y. J. Cheng, W. Hong, and K. Wu, "Millimeter-wave substrate integrated waveguide multibeam antenna based on the parabolic reflector principle," *IEEE Trans. Antennas Propag.*, vol. 56, no. 9, pp. 3055–3058, Sep. 2008, doi: 10.1109/TAP.2008.928812.

[26] Y. Liu, H. Yang, Z. Jin, F. Zhao, and J. Zhu, "A multibeam cylindrically conformal slot array antenna based on a modified Rotman lens," *IEEE Trans. Antennas Propag.*, vol. 66, no. 7, pp. 3441–3452, Jul. 2018, doi: 10.1109/TAP.2018.2829816.

[27] S. Pandi, C. A. Balanis, and C. R. Birtcher, "Design of scalar impedance holographic metasurfaces for antenna beam formation with desired polarization," *IEEE Trans. Antennas Propag.*, vol. 63, no. 7, pp. 3016–3024, Jul. 2015, doi: 10.1109/TAP.2015.2426832.

[28] S. Zhao et al., "Generation of Bessel beam with controllable circular polarization and direction using holographic tensor metasurface," *IEEE Antennas Wireless Propag. Lett.*, vol. 23, pp. 985–989, 2024, doi: 10.1109/LAWP.2023.3340873.



SWARNADIPTO GHOSH (Graduate Student Member, IEEE) received the B.Tech. degree in electronics and communication engineering from the Maulana Abul Kalam Azad University of Technology (MAKAUT), Kolkata, India, in 2022, and the M.Tech. degree in RF and microwave engineering from Indian Institute of Space Science and Technology, Thiruvananthapuram, India, in 2024. He is currently pursuing the joint Ph.D. degree in electrical engineering with the Department of Information Technology, Ghent University, and IMEC, Leuven, Belgium. He has authored over 30 publications, including nine journal articles in peer-reviewed national and international journals and conference proceedings. His research interests include holographic metasurface-based multifunctional antennas, modulated reflect array metasurfaces, beam-steering metasurfaces, leaky wave antennas, and metasurface-integrated wireless power transfer systems. He serves as a reviewer for several esteemed international journals, including IEEE TRANSACTIONS ON ANTENNAS AND PROPAGATION, IEEE ACCESS, *IEEE Microwave Magazine*, *IETE Journal of Research*, *Discover Electronics*, and *Nature Scientific Reports*.



SUBHADRITA GHOSH (Graduate Student Member, IEEE) received the B.Tech. degree in electronics and communication engineering from the University of Engineering and Management, Kolkata, India, in 2023, and the M.Tech. degree in RF and microwave engineering from Indian Institute of Space Science and Technology, Thiruvananthapuram, India, in 2025. She is currently pursuing the Ph.D. degree in electronics and electrical engineering with the Centre for Wireless Innovation, Queen's University Belfast, U.K. She has authored over ten publications, including one journal articles in peer-reviewed international journals and conference proceedings. Her research interests include holographic metasurface-based multifunctional antennas, metasurfaces, beam-steering metasurfaces, leaky-wave antennas. She serves as a reviewer for some esteemed international journals, including IEEE OPEN JOURNAL OF ANTENNAS AND PROPAGATION, IEEE ANTENNAS AND WIRELESS PROPAGATION LETTERS, and *Nature Scientific Reports*.



CHINMOY SAHA (Senior Member, IEEE) received the B.Tech., M.Tech., and Ph.D. degrees in radio physics and electronics from the University of Calcutta, Kolkata, India, in 2002, 2005, and 2012, respectively. He has visited several international universities of repute and having collaborative research with the Royal Military College of Canada, Queen's University, Kingston, ON, Canada. He is currently a Professor with the Department of Avionics, Indian Institute of Space Science and Technology, Thiruvananthapuram, India, and the Department of Space, Government of India. He has more than 170 publications, including 45 journal articles in peer-reviewed national and international journals and conference proceedings, and has authored three books with reputed Cambridge University Press, U.K., and Taylor and Francis, USA. His current research interests include wireless power transfer (WPT) and energy harvesting, channel modeling for wideband (WB)/UWB systems, microwave circuits, engineered materials, metamaterial inspired antennas and circuits, reconfigurable and multifunctional antennas for modern wireless applications, mm-wave THz antennas, and antennas and components for space applications. He is a Senior Member of the International Union of Radio Science and a Life Member of IETE. He has received several prestigious awards that include the Indo-French SRTF Fellowship from the Embassy of France; the National Award "AICTE Visvesvaraya Best Teacher Award 2021" from the Union Education Minister, Government of India; the IETE Prof. SN Mitra Memorial Award 2021; the Outstanding Teacher Award from the Department of Avionics, IIST, in 2019; the National Scholarship from the Ministry of Human Resource Development from Government of India; the Outstanding Contribution Award from the AP-MTT Kolkata Chapter; the Best Contribution Award for Notable Services and Significant Contributions toward the advancements of IEEE and the engineering profession from IEEE Kolkata Section; and several best paper awards in various international conferences. He is the Founding Chair of IEEE MTT-S Kerala Chapter. He has served as the Chair for Antennas and Propagation Chapter of IEEE Kerala Section, from 2018 to 2019. He is a member of the International Committee of AP-S and MTT-S SIGHT and Chapter Activity Committee of IEEE AP-S and a current Region-10 Coordinator of IEEE MTT Society. He is on the board of reviewers of several international journals of repute, including IEEE TRANSACTIONS ON MICROWAVE THEORY AND TECHNIQUES, IEEE TRANSACTIONS ON ANTENNAS AND PROPAGATION, and IEEE ANTENNAS AND WIRELESS PROPAGATION LETTERS. He is an Associate Editor of IEEE ACCESS and *International Journal of RF and Microwave Computer-Aided Engineering* (Wiley) and the Guest Editor-in-Chief for a special issue in *International Journal of RF and Microwave Computer-Aided Engineering*.